

Strain engineering for transition-metal defects in SiC

Benedikt Tissot^{1,*}, Péter Udvarhelyi^{2,3}, Adam Gali^{2,3,4} and Guido Burkard^{1,†}

¹*Department of Physics, University of Konstanz, D-78457 Konstanz, Germany*

²*HUN-REN Wigner Research Centre for Physics, P.O. Box 49, H-1525 Budapest, Hungary*

³*Budapest University of Technology and Economics, Institute of Physics, Department of Atomic Physics, Műegyetem rakpart 3., 1111 Budapest, Hungary*

⁴*MTA-WFK Lendület “Momentum” Semiconductor Nanostructures Research Group, P.O. Box 49, H-1525 Budapest, Hungary*



(Received 30 October 2023; revised 8 January 2024; accepted 30 January 2024; published 20 February 2024)

Transition metal (TM) defects in silicon carbide (SiC) are a promising platform for applications in quantum technology as some of these defects, e.g., vanadium (V), allow for optical emission in one of the telecom bands. For other defects, it was shown that straining the crystal can lead to beneficial effects regarding the emission properties. Motivated by this, we theoretically study the main effects of strain on the electronic-level structure and optical electric-dipole transitions of the V defect in SiC. In particular, we show how strain can be used to engineer the g tensor, electronic selection rules, and the hyperfine interaction. Based on these insights, we discuss optical Lambda systems and a path forward to initializing the quantum state of strained TM defects in SiC.

DOI: [10.1103/PhysRevB.109.054111](https://doi.org/10.1103/PhysRevB.109.054111)

I. INTRODUCTION

A fundamental ingredient for many quantum technologies and experiments is a coherent interface between flying qubits and stationary quantum memories [1–3]. An established set of physical systems with great potential in this domain are so-called color centers, which are defects in solids with optical transitions. Color centers can often additionally be coupled to nearby nuclear spins that lend themselves to quantum memories or long-lived quantum registers.

The most studied color center is the negatively charged nitrogen-vacancy (NV) defect in diamond [4–16] ([17–19] for reviews). Optical initialization and readout of its electron spin state is made feasible by the spin-photon interface via its excited state [20]. Together with a coherent microwave manipulation, optically detected magnetic resonance is feasible in this defect [21]. Efficient coupling to nearby nuclear spins was demonstrated and utilized in long-living quantum memory applications [11,15,16]. Despite its favorable spin and optical properties, contenders for host materials other than diamond are emerging. The most notable is silicon carbide (SiC) with advanced crystal growth [22], defect creation [23,24], and microfabrication techniques readily available [25–28]. These technological advancements improve the scalability [29,30] and magneto-optical properties of several hosted quantum defects, e.g., the negatively charged silicon vacancy [31–33] and the neutral divacancy [34,35].

In this paper, we focus on the transition metal (TM) defects in silicon-carbide (SiC) which have one active electron in a d -like orbital configuration and C_{3v} symmetry. In particular, we investigate vanadium (V) defects, where a V atom replaces

a Si atom of the lattice in the neutral (V^{4+}) charge state. This charge state can be stabilized by tailoring the dopant concentration [36]. In contrast to the defects discussed in the previous paragraph, these V defects in SiC feature a zero-phonon line (ZPL) within the telecom bands, favorable for minimal loss transmission using optical fibers. The focus of previous experiments [36–41] and theory [42–46] for TM defects in SiC was on unstrained defects, however, the knowledge on the external perturbations effecting the magneto-optical properties of the quantum defects is a key ingredient in their applications [47–50]. Note that in the experiment by Cilibrizzi *et al.* [36], small frequency shifts of the crystal field splitting between different regions of the sample were attributed to strain. Strain can be used passively, e.g., to reduce the dispersive readout time in silicon vacancy centers in diamond [51] and to engineer the electronic structure [52] and g tensor [53], or actively to drive spin transitions in NV centers [47] as well as to create a hybrid quantum systems by coupling a mechanical oscillator to defects [54–56].

Motivated by these prospects, in this paper we aim to generalize the effective Hamiltonian to describe TM defects in silicon carbide under strain. To this end, we build on top of previous group-theory based results [43,44] which were in good agreement with previous *ab initio* calculations [42] and experimental findings [36,39–41]. Additionally, we use density functional theory (DFT) calculations to estimate the strain coupling strength for the commonly used vanadium defect in the k site of 4H-SiC [57]. We show how strain in these samples can be used to engineer the optical transition frequency, the g tensor, and transition rules as well as the form of the hyperfine interaction. Based on this, we discuss state preparation and readout as well as microwave control in strained samples.

This paper is organized as follows. We begin by introducing the physical model for the V defect in SiC in Sec. II,

*benedikt.tissot@uni-konstanz.de

†guido.burkard@uni-konstanz.de

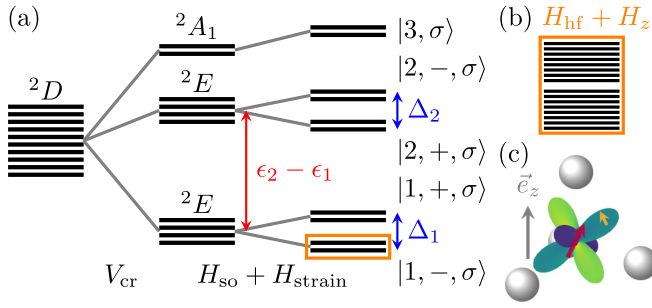


FIG. 1. Sketch of the level structure and atomic configuration at the defect site. (a) Hierarchy leading to the strained electronic structure, where the largest splitting of the D -shell levels occupied by a single electron is due to the crystal field (red arrow), leading to two orbital doublets E and one orbital singlet A_1 , with additional twofold spin degeneracy. The doublets are further split due to the combination of strain and spin-orbit interaction, resulting in the leading-order splitting [see Eq. (14)] between the Kramers doublets (KDs). The KD originating from the orbital singlet A_1 is not further split. Zooming into one of the KDs, (b) reveals the hyperfine structure and Zeeman splitting. (c) Artistic illustration of the D shell electronic orbital of the defect (green and purple), electron spin (yellow), nuclear spin (dark red), and nearest-neighboring sites (gray balls). The gray arrow indicates the crystal axis \vec{e}_z .

including its effective Hamiltonian. Using this model, we combine and compare the effective Hamiltonian and *ab initio* calculations in Sec. III A. Based on these results, we then show the possibility to engineer the g tensor (Sec. III B), selection rules (Sec. III C), and how these can be combined to create a Lambda system for pseudo-spin state preparation (Sec. III D). In Sec. III E, we discuss the influence of strain on the hyperfine interaction and how this influences the possibility to initialize the nuclear spin. We summarize our findings and present our conclusions in Sec. IV.

II. MODEL

A. Defect structure

The defect energy levels, sketched in Fig. 1, can be described by a single electron in an orbital resembling the original atomic d orbital. The $2D$ levels are split by the crystal potential into two orbital doublets $2E$ and one orbital singlet $2A_1$. Due to the spin-orbit interaction and the interaction with an external strain field, the orbital doublets are further split. This results in a level structure made up by five Kramers doublets (KDs) which are pairs of states related to each other by time inversion. We use a group theoretic model in the following to describe the above interactions within an effective Hamiltonian where we additionally calculate selection rules between the KDs, the hyperfine structure of the KDs, and the Zeeman term within each KD. Therein, we calculate the orbital-strain interaction parameters not yet reported in the literature using *ab initio* calculations and also use these to confirm predictions made by the effective Hamiltonian. While we concentrate the *ab initio* calculation to the substitutional vanadium defect at a Si k site in 4H-SiC, the insights of the effective Hamiltonian can be transferred to defects with the

appropriate electronic configuration (one electron in a d -like orbital) and symmetry (C_{3v}) by changing the parameters according to the different configuration.

B. Effective Hamiltonian

We generalize the effective Hamiltonian from Refs. [43,44,46] to additionally include the strain such that the full Hamiltonian is of the form

$$H = H_{\text{TM}} + V_{\text{cr}} + H_{\text{so}} + H_z + H_{\text{nuc}} + H_{\text{el}} + H_{\text{st}}, \quad (1)$$

where the form of the atomic Hamiltonian (H_{TM}), crystal potential V_{cr} , spin-orbit interaction H_{so} , and coupling to magnetic H_z and electric fields H_{el} are discussed in Ref. [43]. The interaction with the central nuclear spin H_{nuc} (of the TM) was derived and analyzed in Ref. [44]. We summarize the form of these terms below and additionally discuss the influence of strain H_{st} within this symmetry-based framework. We note that this approach can only work in the domain where the strain can be viewed as a small perturbation compared to $H_{\text{TM}} + V_{\text{cr}}$. As we show in the following, this restriction does not affect our conclusions, since significant strain effects are demonstrated within this domain. We remark that this domain also covers the strain magnitudes observed in state-of-the-art experiments [36,52,55,58].

In the basis of (orbital) eigenstates $|0\rangle, |\pm_n\rangle$ with $n = 1, 2$ of $H_{\text{TM}} + V_{\text{cr}}$ (introduced in Ref. [43]) and using the corresponding projections onto orbital doublets $P_n = |+_n\rangle\langle+_n| + |-_n\rangle\langle-_n|$ and the projection onto the orbital singlet $P_3 = |0\rangle\langle 0|$, we can write the combined atomic and crystal Hamiltonian as

$$H_{\text{TM}} + V_{\text{cr}} = \sum_{l=1,2,3} \epsilon_l P_l, \quad (2)$$

where ϵ_l are the crystal energies. Here, $l = 1, 2, 3$ labels the three orbital multiplets shown in Fig. 1(a), and we choose ϵ_1 to denote the energy of the lower energy doublet, henceforth referred to as ground state (GS) doublet, such that $\epsilon_2 - \epsilon_1 = \Delta_{\text{cr}}$ denotes the crystal field splitting between the GS and excited state (ES) orbital doublets and $\epsilon_3 - \epsilon_1$ the splitting between the GS orbital doublet and the orbital singlet. We note that within the effective Hamiltonian, $\epsilon_1 = 0$ can be chosen for simplicity. In the following, we describe each part of the Hamiltonian H by its contribution to each of the nine blocks $P_l H P_m$ defined by the three orbital sectors ($l, m = 1, 2, 3$).

Using the projection operators, we can formulate the different blocks of the spin-orbit interaction as

$$P_n H_{\text{so}} P_m = \lambda_{nm}^z S_z \sigma_z + i(n-m) \lambda_{nm}^x (S_x \sigma_y + S_y \sigma_x), \quad (3)$$

$$\langle 0 | H_{\text{so}} | \pm_n \rangle = \lambda_{n3}^x (S_x \pm i S_y), \quad \langle 0 | H_{\text{so}} | 0 \rangle = 0, \quad (4)$$

where $n, m = 1, 2$, σ_k denote the Pauli matrices (here acting between the orbital states $|\pm_n\rangle$), and S_k ($k = x, y, z$) the spin-1/2 operators of the electron in units of \hbar . The spin-orbit coupling constants λ_{nm}^k are in units of energy with this convention.

Another relevant term is the electronic Zeeman interaction due to the spin and angular momentum coupling to an external magnetic field. In the relevant subspaces, it is

given by

$$P_n H_z P_m = r_{nm}^z B_z \sigma_z + \mu_B g_s \vec{B} \cdot \vec{S} \delta_{nm} + i(n-m)r_{nm}^x (B_x \sigma_y + B_y \sigma_x), \quad (5)$$

$$\langle 0 | H_z | \pm_n \rangle = r_{n3}^x (B_x \pm iB_y), \quad \langle 0 | H_z | 0 \rangle = \mu_B g_s \vec{B} \cdot \vec{S}, \quad (6)$$

where we use the electron gyromagnetic ratio $g_s = 2$, the Bohr magneton μ_B , and the coupling constants of the orbital Zeeman term r_{nm}^k .

The nuclear Hamiltonian $H_{\text{nuc}} = H_{\text{hf}} + H_{\text{zn}}$ (for TM defects with nonzero nuclear spin) is made up by the hyperfine interaction H_{hf} and the nuclear Zeeman interaction $H_{\text{zn}} = \mu_N g_N \vec{B} \cdot \vec{I}$ with the nuclear spin operator \vec{I} in units of \hbar , the nuclear magneton μ_N , and nuclear g factor g_N . As the nuclear Zeeman term is proportional to the identity operator $\mathbb{1}$ in the electronic subspace, it can be straightforwardly incorporated. Following Ref. [44] and accommodating to the notation employed in this paper, the hyperfine interaction projected onto the relevant subspaces is

$$\begin{aligned} P_n H_{\text{hf}} P_m = & a_{nm}^z S_z I_z + \frac{a_{nm}^z}{2} (S_+ I_- + S_- I_+) - \frac{a_{nm}^x}{2} [\sigma_- S_+ I_+ + \sigma_+ S_- I_-] \\ & + \frac{1}{2} a_{nm}^x [S_z (\sigma_+ I_+ + \sigma_- I_-) + (S_+ \sigma_+ + S_- \sigma_-) I_z] + a_{nm}^z I_z \sigma_z + \frac{a_{nm}^x}{2} (n-m) (\sigma_+ I_+ - \sigma_- I_-), \end{aligned} \quad (7)$$

$$\langle 0 | H_{\text{hf}} | \pm_n \rangle = a_{n3}^x I_{\pm} \pm a_{n3}^x S_{\mp} I_{\mp} \mp a_{n3}^x [S_z I_{\pm} + S_{\pm} I_z], \quad \langle 0 | H_{\text{hf}} | 0 \rangle = a_{33}^z S_z I_z + \frac{1}{2} a_{33}^z (S_+ I_- + S_- I_+), \quad (8)$$

where we use the ladder operators $O_{\pm} = O_x \pm iO_y$ with $O = \sigma, S, I$ as well as the set of hyperfine coupling parameters a_{nm}^k , $a_{nm}^{k'}$, and $a_{nm}^{k''}$.

The effect of an applied electric field \vec{E} can be described by

$$P_n H_{\text{el}} P_m = \mathcal{E}_{nm}^z E_z \mathbb{1} + \mathcal{E}_{nm}^x (\sigma_x E_x - \sigma_y E_y), \quad (9)$$

$$\langle 0 | H_{\text{el}} | \pm_n \rangle = \mp \mathcal{E}_{n3}^x (E_x \pm iE_y), \quad \langle 0 | H_{\text{el}} | 0 \rangle = \mathcal{E}_{33}^z E_z, \quad (10)$$

with the coupling strengths \mathcal{E}_{nm}^k .

Lastly, we turn to the strain Hamiltonian. In our model, we start with a product space of orbital and spin components, such that we can incorporate the strain interaction within the orbital subspace. Its competition with the spin-orbit interaction gives rise to a complex interplay within the KDs. To describe it, we use the assignment of the different strain elements to irreducible representations of C_{3v} [47] which then couple to the corresponding orbital operator, i.e., the strain components transforming like the basis $\{x, y\}$ of the irreducible representation E couple to operators of the form of x and y , while the strain components transforming like the basis z of A_1 couple to operators of the form of z . With these considerations, the strain Hamiltonian

$$P_n H_{\text{st}} P_m = \epsilon_{nm}^z \mathbb{1} + (\sigma_x \epsilon_{nm}^x - \sigma_y \epsilon_{nm}^y), \quad (11)$$

$$\langle 0 | H_{\text{st}} | \pm_n \rangle = \mp (\epsilon_{n3}^x \pm i\epsilon_{n3}^y), \quad \langle 0 | H_{\text{st}} | 0 \rangle = \epsilon_{33}^z, \quad (12)$$

has a similar structure as the coupling to electric fields but potentially leads to a much larger contribution. Here, we use the reduced components of the strain tensor, organized by symmetry, $\epsilon_{nm}^x = s_{nm}^x \epsilon_{xz} + s_{nm}^x \frac{\epsilon_{yy} - \epsilon_{xx}}{2}$, $\epsilon_{nm}^y = s_{nm}^y \epsilon_{yz} + s_{nm}^y \epsilon_{xy}$, and $\epsilon_{nm}^z = s_{nm}^z \epsilon_{zz} + s_{nm}^z \frac{\epsilon_{xx} + \epsilon_{yy}}{2}$. In contrast to the coupling to electric (and magnetic) fields, the tensorial form of the strain manifests itself in the presence of multiple strain elements pertaining to the same irreducible representation. These elements can also have different coupling constants s_{nm}^k and

$s_{nm}^{k'}$ leading to more degrees of freedom than a coupling to vectors.

For concreteness, we focus on the vanadium defect in the k site of 4H-SiC in the following. We use the already known combinations of parameters and additionally estimate the magnitude of the strain coupling constants using DFT calculations. Many relevant parameters without strain can be found in our previous works [43,44,46] which are symmetry adapted from Refs. [40,41], including their values for other defects. Because the telecom transition is attributed to lie between two orbital doublets [40,44] and strain can mix different KDs pertaining to the same orbital doublet but not the orbital singlet in the leading order, we focus our discussion on the projection onto the orbital doublets in the following. Note that we also consider the orbital singlet while calculating higher order corrections in Appendix C.

III. RESULTS

In a first step, we investigate the electronic structure following from an externally applied, uniaxial, and static strain. The remaining terms in the Hamiltonian will be discussed afterwards, omitting the discussion of static electric fields as they couple weakly to the defect compared to strain and magnetic fields and the symmetry-based electric-field coupling Hamiltonian [Eqs. (9) and (10)] is similar to the strain Hamiltonian [Eqs. (11) and (12)].

Referring to the absence of an external electromagnetic field as zero field, we define the electronic zero-field Hamiltonian as $H_{\text{ezf}} = H_{\text{TM}} + V_{\text{cr}} + H_{\text{so}} + H_{\text{st}}$. Projected onto one of the doublets ($n = 1, 2$), the electronic zero-field Hamiltonian is

$$P_n H_{\text{ezf}} P_n = (\epsilon_n + \epsilon_{nn}^z) \mathbb{1} + \lambda_{nn}^z S_z \sigma_z + (\sigma_x \epsilon_{nn}^x - \sigma_y \epsilon_{nn}^y), \quad (13)$$

where we take the crystal-field splitting to be the dominant contribution, i.e., $|\epsilon_l - \epsilon_m| \gg \lambda_{ij}^k, \epsilon_{ij}^k$ with $l \neq m, l, m, i, j = 1, 2, 3$, and $k = x, y, z$. Furthermore, we investigate the

domain where the magnetic field is weak compared to the spin-orbit coupling, as is relevant for most experimental and technological applications. Therefore, we begin by diagonalizing the Hamiltonian Eq. (13), leading to the eigenvalues

$$E_{n,\pm} = \epsilon_n + \epsilon_{nn}^z \pm \frac{1}{2} \text{sign}(\lambda_{nn}^z) \Delta_n, \quad (14)$$

with the combined spin-orbit and strain splitting $\Delta_n = \sqrt{(\lambda_{nn}^z)^2 + 4(\epsilon_{nn}^x)^2 + 4(\epsilon_{nn}^y)^2}$. As it splits the orbital doublet into two KDs (made up by two pseudospins), we refer to Δ_n as the orbital splitting. These energies are doubly degenerate in agreement with Kramers' theorem, as time-reversal symmetry is still preserved for this static Hamiltonian, despite the (potential) spatial symmetry breaking due to strain. The corresponding eigenstates are

$$|n, \pm, \sigma\rangle = \cos(\theta_n/2) |\pm\sigma_n\rangle |\sigma\rangle \pm \sin(\theta_n/2) \exp(\mp i\sigma\varphi_n/2) |\mp\sigma_n\rangle |\sigma\rangle, \quad (15)$$

where $\sigma = \uparrow, \downarrow$ denotes the spin and is also used as $\sigma = \pm$ to achieve a concise notation. The x - and y -like components of the strain coupling compete with each other and with the spin-orbit coupling, leading to the mixing angles $\tan(\theta_n) = 2\epsilon_{nn}^x \sqrt{1 + (\epsilon_{nn}^y/\epsilon_{nn}^x)^2} / \lambda_{nn}^z$ and $\tan(\varphi_n) = \epsilon_{nn}^y/\epsilon_{nn}^x$. Without strain, the C_{3v} symmetry of the defect is intact, yielding the KDs Γ_4 and $\Gamma_{5/6}$ for the $|n, -, \sigma\rangle$ and $|n, +, \sigma\rangle$ KDs, respectively.

A. *Ab initio* calculations

We perform *ab initio* calculations on the defect system to determine its strain-orbital coupling strengths. For the calculation details, see Appendix A. The defect structure shows C_{3v} point symmetry owing to the axial crystal field of the 4H polytype. It introduces a double-degenerate $e^{(1)}$ orbital inside the band gap, occupied by a single electron and two empty orbital levels ($e^{(2)}$ and a_1) which are localized inside the conduction band in the 2E ground-state electronic configuration. The lowest energy excitation promotes the electron between the different e levels, sinking the $e^{(2)}$ orbital inside the band gap, we sketch the level structure in Fig. 2. The calculated ZPL energy of 0.91 eV is in reasonable agreement with experiments [40]. We note that Jahn-Teller instabilities are suppressed in the calculations by a smeared occupation in the e orbital subspace, describing a dynamically averaged system in the unperturbed solution and strain perturbation is applied to this high-symmetry system.

First, we determine the s_{nn}^k orbital-strain coupling constants, without spin-orbit coupling taken into account, in both the ground and first excited state of the defect. To this end, we apply strain with a magnitude of up to 0.02 and fit a linear response for the orbital-level splitting energy and the ZPL energy in the case of E and A_1 strain components, respectively. The coupling coefficients are extracted as the fitted slope. Within the margin of error (see Appendix A), the slope for strains transforming together agree and are predicted to have the same s_{nn}^k by the effective Hamiltonian, such that we will use their average in the following. The calculated values are collected in Table I, where we additionally assigned the signs based on the discussion in Appendix B. To confirm the agreement between the effective Hamiltonian and the *ab initio*

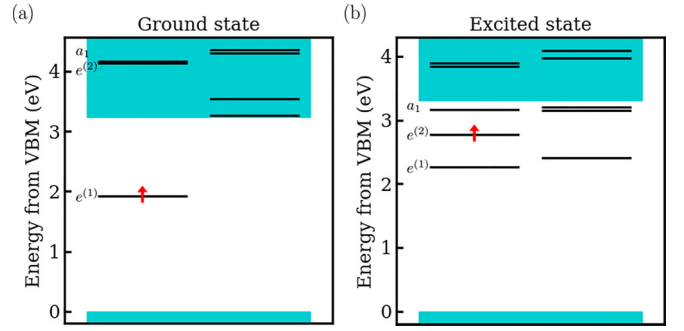


FIG. 2. Kohn-Sham level structure of the substitutional vanadium defect in 4H-SiC calculated with the HSE06 DFT functional. The two sets of levels correspond to the two spin channels in the spin-polarized calculation. Occupation and spin polarization is indicated by red arrows. (a) The ground-state doublet originates from a doubly degenerate orbital inside the gap. (b) Promoting this electron to the higher lying double degenerate level creates localized excitation inside the band gap.

calculations as well as the extrapolation of using the purely orbital calculations to extract the strain coupling constants s_{nn}^k , we use these combined with the spin-orbit splitting in the absence of strain predicted by the *ab initio* calculation given by about $\lambda_{11}^z/h = 1112$ GHz to calculate the ground-state energy splitting and compare them to simulations combining strain and the spin-orbit interaction, see Fig. 3. The spin-orbit splitting calculated using DFT turns out to be about twice the experimentally measured value of 529 GHz [40] in agreement with a Ham reduction factor of about 0.6 [42].

For this reason, we will use the numerically determined strain coupling constants but use experimentally determined parameters from the literature where available. In particular, we compare the mixing angle as well as the combined spin-orbit and strain splitting as functions of strain components transforming according to the x basis element of the irreducible representation E (of C_{3v}) in the GS and ES doublets in Fig. 4 using the experimentally determined spin-orbit splittings $\lambda_{11}^z/h = 529$ GHz and $\lambda_{22}^z/h = -181$ GHz [40], where we assigned the signs based on the level ordering [44]. Figure 4 shows that the splittings of the ES and GS diverge

TABLE I. Calculated strain-orbital coupling coefficients extracted from the linear perturbation model of the orbital-level splitting and ZPL energies from DFT. We average the coupling of elements pertaining to the same irreducible representation, as they are predicted to be the same by the Wigner-Eckart theorem and agree within numerical accuracy between the original DFT results; see Table II. The signs are assigned according to Appendix B. For the effective Hamiltonian, we choose to use $s_{11}^z = s_{11}^x = 0$ and assign the slope of the energy difference from the DFT calculations to s_{22}^z and s_{22}^x .

n	k	s_{nn}^k (h THz/strain)	$s_{nn}^{k'}$ (h THz/strain)
1	x	251 ± 1	230 ± 3
2	x	-138 ± 6	-204 ± 3
2	z	459 ± 24	305 ± 19

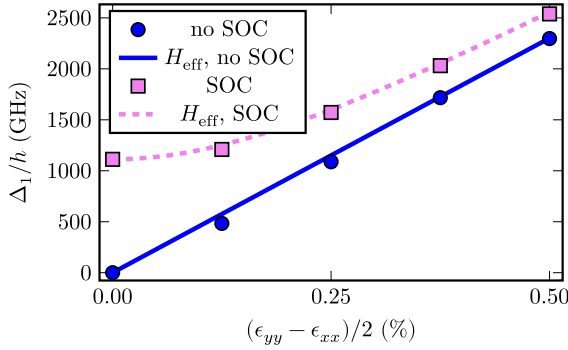


FIG. 3. Ground-state orbital splitting Δ_1 as a function of strain $\epsilon_{yy} - \epsilon_{xx}$ comparing the effective Hamiltonian and DFT calculations. The blue line (dots) shows the linear dependence of the orbital splitting in the absence of spin-orbit splitting obtained from the effective Hamiltonian (from DFT). The pink dashed line (squares) show the combined spin-orbit and strain splitting from the effective Hamiltonian (from DFT), following the prediction, Eq. (14). The effective Hamiltonian uses the zero-strain spin-orbit splitting (extracted from the DFT) and fitted s_{11}^z (see Table I).

more for $\epsilon_{yy} - \epsilon_{xx}$ strain than for ϵ_{xz} . The mixing angle between the strain types is also different where it increases faster for ϵ_{xz} strain and in all cases approach the asymptotic value of $\pi/2$ which corresponds to maximal mixing of the unstrained KDs, see Eq. (15).

The linear dependence of Eq. (14) on z -type strain, i.e., ϵ_{zz} and $\epsilon_{xx} + \epsilon_{yy}$, combined with the nonzero difference of the coupling constants between the GS and ES from the *ab initio* calculation (see Table I) implies that z -type strain can be used to tune the optical transition frequency, i.e., the crystal field splitting. This is possible while keeping the selection rules intact as z -type strain conserves the defect's C_{3v} symmetry. Within the effective Hamiltonian, we choose to use

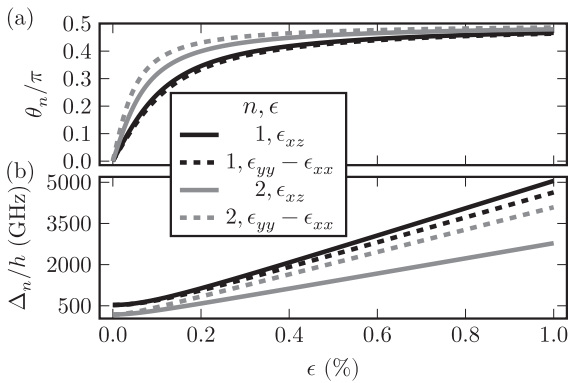


FIG. 4. Behavior of Kramers doublets pertaining to the same orbital doublet under strain ϵ at zero field. (a) Strain mixing angle θ_n [see Eq. (15)] and (b) orbital energy splitting [see Eq. (14)] as a function of ϵ . The plots show an increase in both mixing and splitting with increasing strain. The symmetric KDs Γ_4 and $\Gamma_{5/6}$ are fully mixed for highly strained samples. Furthermore, we note that the mixing angle is antisymmetric, while the energy splitting is symmetric when inverting the sign of the strain. We use the coupling constants in Table I as well as $\lambda_{11}^z/h = 529$ GHz and $\lambda_{22}^z/h = -181$ GHz.

$s_{11}^z = s_{11}^{z'} = 0$ because the overall energy shift can be set arbitrarily and only the energy differences contained in the effective Hamiltonian carry physical meaning. We assign the full difference of the coupling of the ES and GS orbital doublets extracted from the *ab initio* calculation to the parameters s_{22}^z and $s_{22}^{z'}$.

B. Engineering the g tensor

Projecting onto the $n(=1, 2), \pm$ KD (spanned by the states $|n, \pm, \sigma\rangle$ with $\sigma = \uparrow, \downarrow$), we calculate the leading-order Zeeman term

$$H_{n,\pm}^z = \mu_B g_{n,\pm}^z \tilde{S}_z B_z + \mu_B g_{n,\pm}^x \begin{pmatrix} \tilde{S}_x \\ \tilde{S}_y \end{pmatrix} \begin{pmatrix} \cos(\varphi_n) & \pm \sin(\varphi_n) \\ \mp \sin(\varphi_n) & \cos(\varphi_n) \end{pmatrix} \begin{pmatrix} B_x \\ B_y \end{pmatrix}, \quad (16)$$

with the effective g factors $g_{n,\pm}^z = g_s \pm 2r_{nn}^z \cos(\theta_n)$ and $g_{n,\pm}^x = \pm g_s \sin(\theta_n)$, where \tilde{S}_k is the $k = x, y, z$ pseudospin ($1/2$) operator for the KD. From this expression, it is evident that using x, y strain enables coupling to perpendicular magnetic fields such that quantum gates relying on $S_{x,y}$ operators become possible using microwave drives; the coupling $g_{n,\pm}^x$ to $S_{x,y}$ vanishes in the leading order in the absence of strain ($\theta_n = 0$). Furthermore, y -type strain leads to an effective rotation of the spin in the x, y plane regarding an external magnetic field.

As we previously showed in the absence of strain [43], in the presence of strain the g factors are also influenced by (combined) higher orders of the strain and spin-orbit interactions between different orbital subspaces. We calculate the (second-order) correction using a Schrieffer-Wolf transformation treating $H_{so} + H_{st}$ as the perturbation. In Appendix C, we show how to derive the correction for $g_{n,\pm}^z$ for purely x -type strain. These are in agreement with previous unstrained results. Using the insights of the higher order, we use $r_{nn}^z = \sum_{s=\pm} |g_s - g_{n,s}^{z,0}|/4$ with the experimentally determined $g_{n,s}^{z,0}$ at zero strain of the same doublet n and attribute the remaining individual deviation between $g_{n,s}^{z,0}$ and $g_{n,s}^z$ to a common deviation from g_s due to the second-order term. With this consideration and using the g factors [40,41,44], we find $r_{11}^z = 0.103$ for vanadium defects in the k site in 4H-SiC (and the second-order correction is 0.046). Using these parameters, we show the evolution of the parallel and perpendicular g factors as a function of the strain mixing angle θ_1 for the ground-state KD in Fig. 5 where we do not include the small second-order correction. This figure makes it readily visible that as $r_{11}^z \ll g_s$, the parallel g factor changes little compared to the perpendicular g factor. The perpendicular g factor $g_{1,-}^x$ varies between 0 in the absence of strain up to $\pm g_s = \pm 2$ while the parallel g factor $g_{1,-}^z$ only shows a marginal deviation from $g_s = 2$.

C. Engineering optical transitions

After discussing the interaction with magnetic fields, which is essential to split the pseudospin levels and for microwave control, we investigate the leading-order electric dipole transition matrix elements in this subsection. These

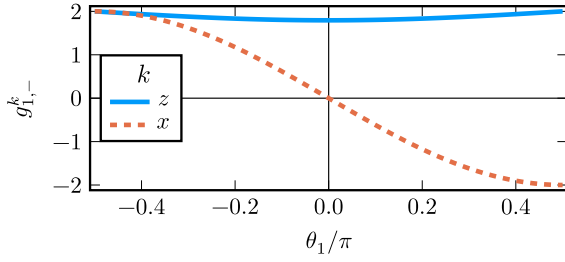


FIG. 5. Parallel and perpendicular g-tensor elements as a function of the strain mixing angle θ_1 for the GS KD. In the absence of strain, the perpendicular g factor vanishes and increases (decreases) for positive (negative) strain mixing angles θ_1 . The parallel g factor only slightly varies around the value of 2. Parameters used for this plot are $g_s = 2$ and $r_{11}^z = 0.103$.

matrix elements are important to characterize the interaction with optical fields. In the absence of strain, all leading-order transitions conserve the spin $\langle n, \pm, \sigma | H_{el} | m, \pm, -\sigma \rangle = 0$ and $\langle n, \pm, \sigma | H_{el} | 3, -\sigma \rangle = 0$ [43]. We refer to Refs. [43,46] for a summary of the selection rules for intact C_{3v} symmetry. For simplicity, we focus on the transitions between the 1, $-$ KD and the two 2, \pm KDs under the (leading-order) influence of strain. To this end, we calculate

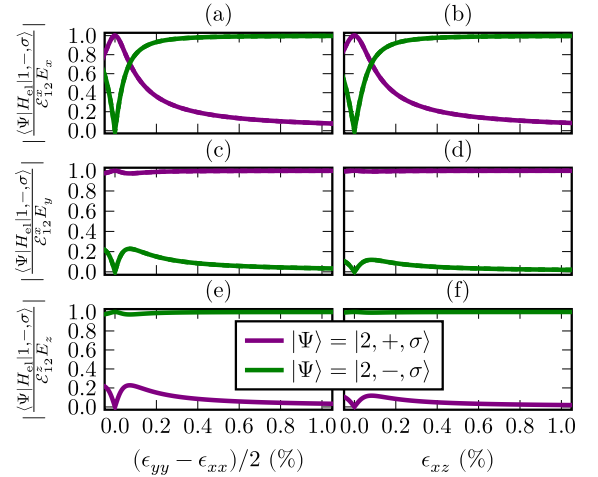


FIG. 6. Electric dipole transition matrix elements as a function of x -type strain for linear polarized drives. The color (see legend) encodes the target ES $|2, \pm, \sigma\rangle$ that couples pseudospin conserving to the GS KD $|1, -, \sigma\rangle$. Rows (a), (b); (c), (d); and (e), (f) show the selection rules for E_x , E_y , E_z , respectively. Columns (a), (c), (e) and (b), (d), (f) correspond to the two different x -type strains $(\epsilon_{yy} - \epsilon_{xx})/2$ and ϵ_{xz} . The pseudospin σ is encoded in the line style solid (dashed) for \uparrow (\downarrow) but is not visible as the lines are aligned. We use the same parameters as in Fig. 4.

$$\begin{aligned} \langle 2, +, \sigma | H_{el} | 1, -, \sigma \rangle \sigma e^{-\sigma i(\varphi_1 + \varphi_2)/2} &= E_z \mathcal{E}_{12}^z \left[e^{i(\varphi_2 - \varphi_1)/2} \cos\left(\frac{\theta_1}{2}\right) \sin\left(\frac{\theta_2}{2}\right) - e^{-i(\varphi_2 - \varphi_1)/2} \cos\left(\frac{\theta_2}{2}\right) \sin\left(\frac{\theta_1}{2}\right) \right] \\ &+ \mathcal{E}_{12}^x \left[(\sigma E_x + iE_y) e^{-\sigma i(\varphi_2 + \varphi_1)/2} \cos\left(\frac{\theta_1}{2}\right) \cos\left(\frac{\theta_2}{2}\right) + (-\sigma E_x + iE_y) e^{\sigma i(\varphi_2 + \varphi_1)/2} \sin\left(\frac{\theta_1}{2}\right) \sin\left(\frac{\theta_2}{2}\right) \right], \end{aligned} \quad (17)$$

$$\begin{aligned} \langle 2, -, \sigma | H_{el} | 1, -, \sigma \rangle e^{\sigma i(\varphi_2 - \varphi_1)/2} &= E_z \mathcal{E}_{12}^z \left[e^{\sigma i(\varphi_2 - \varphi_1)/2} \cos\left(\frac{\theta_1}{2}\right) \cos\left(\frac{\theta_2}{2}\right) + e^{-\sigma i(\varphi_2 - \varphi_1)/2} \sin\left(\frac{\theta_2}{2}\right) \sin\left(\frac{\theta_1}{2}\right) \right] \\ &+ \mathcal{E}_{12}^x \left[(-E_x - \sigma iE_y) e^{-\sigma i(\varphi_2 + \varphi_1)/2} \cos\left(\frac{\theta_1}{2}\right) \sin\left(\frac{\theta_2}{2}\right) + (-E_x + \sigma iE_y) e^{\sigma i(\varphi_2 + \varphi_1)/2} \sin\left(\frac{\theta_1}{2}\right) \cos\left(\frac{\theta_2}{2}\right) \right]. \end{aligned} \quad (18)$$

Similar expressions can be analogously calculated for other transitions. We show in Fig. 6 how the electric dipole transition matrix elements evolve as a function of the x -type strain elements ϵ_{xz} and $(\epsilon_{yy} - \epsilon_{xx})/2$. This figure underlines that there are domains where these types of strain enable multiple simultaneous transitions and that strain can significantly impact the selection rules of the defect. The strongest change of the selection rules visible in Fig. 6 is the complete inversion of dipole coupling strength to the GS via E_x polarized fields between the ES KDs under x strain. Combined with the influence on E_y , we conclude that the circular polarization selection rules in the absence of strain [46] become linear polarization rules in suitably strained samples. For example, in Fig. 6 it can be seen that the transition $|1, -, \sigma\rangle \leftrightarrow |2, +, \sigma\rangle$ becomes primarily susceptible to E_y in the presence of strong strain. We can generalize this by considering that for strong (positive) strain $\theta_1, \theta_2 \approx \pi/2$, such that we find

$$\langle 2, +, \sigma | H_{el} | 1, -, \sigma \rangle \sigma e^{-\sigma i(\varphi_1 + \varphi_2)/2} = iE_z \mathcal{E}_{12}^z \sin\left(\frac{\varphi_2 - \varphi_1}{2}\right) - i\mathcal{E}_{12}^x \left[E_x \sin\left(\frac{\varphi_2 + \varphi_1}{2}\right) - E_y \cos\left(\frac{\varphi_2 + \varphi_1}{2}\right) \right]. \quad (19)$$

Figure 6 and the above expressions directly show that we can generate an orbital three-level system in the V configuration where one GS KD couples to two ES KDs in the presence of strain. Considering the equivalent structure of the two doublets, we infer that an orbital Lambda (Λ) system can be created analogously.

Because even in the presence of strain the leading-order transitions conserve the pseudospin, the spin-conserving transitions to the ES are cyclic if the pseudospins inside the KDs are not mixed. These cycling transitions are used in many platforms for spin readout [59–63]. Since the coupling to a magnetic field aligned with the crystal axis (\vec{e}_z) is diagonal [see Eq. (16)], the pseudospins are pure for such a magnetic field. Therefore, the application of a static magnetic field perfectly aligned with the crystal axis, splitting the spin levels without mixing them, enables spin readout even in the presence of strain.

D. Pseudospin polarization in a highly strained system

While one possible way to initialize a state is a projective measurement, another approach established in a wide range of platforms is coherent population trapping [7,12–14,64–67]. This approach relies on a Λ system, but in the case of the V defect in SiC, all the leading order transitions conserve the pseudospin of the KDs. For this reason, different hyperfine interactions of KDs [46], additional fields, or higher-order transition rules are needed to polarize the electron spin. Higher orders can be investigated using a Schrieffer-Wolff transformation but are not discussed here for simplicity (see Appendix C for the case with strain or Ref. [43] for the case without strain).

Instead, we briefly outline how the combination of strain and a static magnetic field can be used to set up an optical Λ system. In particular, we propose combining x -type strain, leading to $\theta_1 \neq 0$ and a magnetic field in the xz plane (with nonvanishing x, z components). In this case, the KD's Zeeman terms [see Eq. (16)] are $H_{n,\pm,z} = \mu_B g_{n,\pm}^z \tilde{S}_z B_z + \mu_B g_{n,\pm}^x \tilde{S}_x B_x$, which is diagonalized by the states

$$|n, \pm, \tilde{\sigma}\rangle = \cos(\phi_{n,\pm}/2) |n, \pm, \sigma\rangle + \sigma \sin(\phi_{n,\pm}/2) |n, \pm, -\sigma\rangle, \quad (20)$$

with the corresponding eigenvalues

$$E_{n,\pm,\tilde{\sigma}}^z = \sigma \mu_B g_{n,\pm}^z B_z \sqrt{1 + (g_{n,\pm}^x B_x)^2 / (g_{n,\pm}^z B_z)^2}, \quad (21)$$

and the angles $\phi_{n,\pm} = \arctan[g_{n,\pm}^x B_x / g_{n,\pm}^z B_z]$. With this, an optical Λ system made up by the two GSs $|1, -, \tilde{\sigma}\rangle$ ($\sigma = \uparrow, \downarrow$) and one of the ESs becomes feasible. As an example, we calculate the electric dipole matrix element between the GS and the ES $|2, +, \tilde{\downarrow}\rangle$,

$$\begin{aligned} \langle 1, -, \tilde{\sigma} | H_{el} | 2, +, \tilde{\downarrow} \rangle &= [\cos(\phi_{1,-}/2) \delta_{\sigma,\downarrow} + \sin(\phi_{1,-}/2) \delta_{\sigma,\uparrow}] \cos(\phi_{2,+}/2) \langle 1, -, \downarrow | H_{el} | 2, +, \downarrow \rangle \\ &+ [\sin(\phi_{1,-}/2) \delta_{\sigma,\downarrow} - \cos(\phi_{1,-}/2) \delta_{\sigma,\uparrow}] \sin(\phi_{2,+}/2) \langle 1, -, \uparrow | H_{el} | 2, +, \uparrow \rangle, \end{aligned} \quad (22)$$

with the spin-conserving matrix elements according to Eq. (17). These selection rules also imply that the corresponding decay processes become allowed. Combined, this enables the preparation of a pseudospin state of the GS KD in the presence of strain.

The readout of the qubit discussed in the previous section relied on cyclic transitions. To make the transitions highly cyclic on demand after using the Λ system, we can target $\phi_{n,\pm} = 0$ [see Eqs. (20) and (22)]. This can be achieved either by switching the perpendicular component of the magnetic field on and off (e.g., by changing the relative alignment of the magnetic field) or by modulating the perpendicular g -tensor component via the strain [52,54,56] (see Fig. 5). Note that the adiabatic modulation can be sped up by shortcut to adiabaticity approaches like counteradiabatic driving [68–70].

E. Hyperfine interaction in strained KDs

After the detailed discussion of the interplay of the electronic structure of TM defects in SiC with strain, we now proceed to the hyperfine structure of the KDs in the presence of strain. The Hamiltonian of the hyperfine interaction [Eqs. (7) and (8)] projected onto the strained KDs [Eq. (15)] is

$$\begin{aligned} H_{n,\pm}^{\text{hf}} &= \tilde{S}_z \left[a_{n,\pm}^{zz} I_z \pm \frac{a_{n,\pm}^{zx}}{2} (e^{i\varphi_n} I_- + e^{-i\varphi_n} I_+) \right] \\ &+ \frac{1}{2} [e^{-i(1\pm 1)\varphi_n} \tilde{S}_- (a_{n,\pm}^{xy} I_- + a_{n,\pm}^{xx} e^{i\varphi_n} I_+ + a_{n,\pm}^{xz} e^{2i\varphi_n} I_z) \\ &+ \text{H.c.}], \end{aligned} \quad (23)$$

with the hyperfine coupling constants $a_{n,\pm}^{zz} = a_{nn}^z \pm 2a_{nn}'' \cos(\theta_n)$ and $a_{n,\pm}^{zx} = a_{nn}^x \sin(\theta_n)$, $a_{n,\pm}^{xy} = -a_{nn}^{xy} [1 \mp \cos(\theta_n)]$, $a_{n,\pm}^{xz} = a_{nn}^{xz} [1 \pm \cos(\theta_n)]$, and $a_{n,\pm}^{xx} = \pm a_{nn}^{xx} \sin(\theta_n)$.

We extract the parameters from the literature values (determined at zero strain) [40,41,44,46] using the following relations by comparing the predicted forms for $\theta_n = 0$. The average (quarter of the difference) of $a_{n,\pm}^{zz}$ between the KDs \pm pertaining to the same doublet n yields $a_{nn}^z = \sum_{\sigma=\pm} a_{n,\sigma}^{zz} / 2$ ($a_{nn}'' = \sum_{\sigma=\pm} \sigma a_{n,\sigma}^{zz} / 4$). The components a_{nn}^x and a_{nn}^{xy} are fully given by $-a_{n,-}^{xy} / 2$ and $a_{n,+}^{xz} / 2$, respectively. We plot the coupling constants of the GS KD $|1, -, \sigma\rangle$ as a function of the GS strain mixing angle θ_1 in Fig. 7, where we assume $a_{nn}' = a_{nn}^z$. Figure 7 shows that due to the symmetry breaking, additional hyperfine elements become nonzero compared with the case of intact symmetry ($\theta_n = 0$).

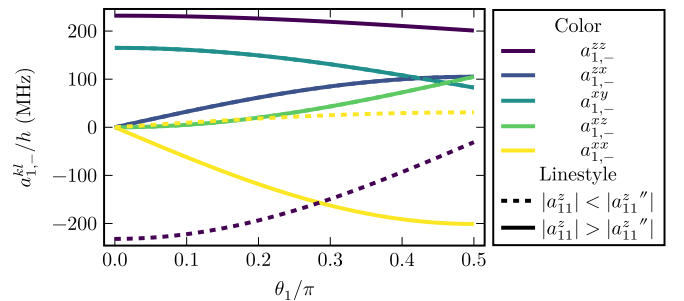


FIG. 7. Hyperfine tensor elements of the GS KD as functions of the strain mixing angle θ_1 . The different colors correspond to the different hyperfine tensor elements (see legend). The solid lines correspond to the case where the orbital hyperfine interaction dominates over the Fermi contact and anisotropic hyperfine interaction and the dashed lines to the reverse. For most elements, both cases align but they significantly differ for $a_{1,-}^{zz}$ and $a_{1,-}^{xx}$. We use the parameters $a_{1,-}^x/h = -82.55$ MHz, $a_{1,-}^{xy}/h = 105$ MHz, $a_{1,-}^{xz}/h = a_{1,-}^{xz}/h = 201$ MHz (-31 MHz) $a_{1,-}^{zz}/h = -15.5$ MHz (100.5 MHz) for the solid (dashed) lines.

While the magnitudes of the different components of the two GS KDs and the lower ES KD are agreed upon within several works [40,41,44,46,71] and thereby enabled the independent determination of the relative sign of the lowest ES and GS [36], the relative sign between the KDs of the same doublet does not have this support. Therefore, we show in Fig. 7 two possible configurations, one for opposite signs (here, $a_{1,-}^{zz} < 0 < a_{1,+}^{zz}$ for $\theta_1 = 0$), where the orbital hyperfine dominates the diagonal interaction and one for the same signs (here, $0 < a_{1,-}^{zz}, a_{1,+}^{zz}$) where the anisotropic hyperfine and Fermi contact interaction are dominant. The vastly different strain dependencies of the zz strain coupling elements for the different signs shows that by measuring this dependence (for example, by using a strong, constant magnetic field), it is possible to determine the relative signs of the hyperfine tensor of the GS KDs without using direct transitions between those. This would then give us insight into whether the $|a_{nn}^z|$ or $|a_{nn}^x|$ is dominant, where the former stems from the anisotropic and Fermi contact terms and the latter from the orbital angular momentum interacting with the nuclear spin. Therefore, such a measurement would determine which of these interactions is prevalent.

In the previously proposed nuclear spin-polarization protocol [46], unstrained samples were considered. Fundamentally, the different forms of the hyperfine coupling between the KDs were devised to a driven dissipative protocol to polarize the nuclear spin. In this protocol, spin-flipping transitions are driven in combination with spin-conserving decays, leading to the polarization of nuclear and electronic spin. We expect this protocol to be possible if the (x, y) strain is sufficiently small such that the GS are dominated by the hyperfine terms $\propto a_{1,-}^{zz}, a_{1,-}^{xy}$ and the ES by the terms $\propto a_{2,+}^{zz}, a_{2,+}^{xz}$. This can be estimated using the strain mixing angles θ_n for $n = 1, 2$ [see Eq. (15)] and Figs. 7 and 4.

On the other hand, for highly (x, y) strained samples, one has a non-negligible θ_n . In this case, one can apply a strong magnetic field along the crystal axis to suppress the hyperfine interaction terms $\propto \tilde{S}_-, \tilde{S}_+$. In this case, the quantization

axis of the nuclear spin is tilted, depending on the KD. This is immediately visible by investigating a single pseudospin manifold,

$$\langle n, \pm, \sigma | H | n, \pm, \sigma \rangle \approx E_{n,\pm,\sigma} + \left(\mu_N g_N B_z + \frac{\sigma}{2} a_{n,\pm}^{zz} \right) I_z \pm \frac{\sigma}{2} a_{n,\pm}^{zx} [\cos(\varphi_n) I_x - \sin(\varphi_n) I_y], \quad (24)$$

with the electronic energy $E_{n,\pm,\sigma}$ and where the magnetic field along z direction suppresses the off-diagonal terms. By first applying a rotation around the z axis by the angle $-\varphi_n$ and then a rotation around the y axis with the angle $\pm \arctan[(\sigma \mu_N g_N B_z + a_{n,\pm}^{zz})/a_{n,\pm}^{zx}]$, we diagonalize this manifold, yielding the diagonal hyperfine term in the rotated basis:

$$\frac{1}{2} \sqrt{(a_{n,\pm}^{zx})^2 + (2\mu_N g_N B_z + \sigma a_{n,\pm}^{zz})^2} I_z. \quad (25)$$

The rotations reflect that the nuclear spin experiences a strain, pseudospin, and KD-dependent principal axis tilt. Independent of the pseudospin, it is possible to drive a (pseudospin) conserving transition to an ancillary state (AS) n, \pm, σ with a different principal axis tilt incrementally increasing the nuclear-spin polarization. This enables nuclear polarization. For simplicity, we will discuss an approach based on purely x -type strain, i.e., $\theta_i \neq 0$ and $\varphi_i = 0$. Transforming any KD pseudospin σ manifold into the diagonal basis of the GS KD down state $(1, -, \downarrow)$, we find that we need to replace $I_z \rightarrow \cos(\Delta\varphi) I_z + \sin(\Delta\varphi) I_x$ in Eq. (25) with the relative axis tilt angle $\Delta\varphi = \arctan[(-\mu_N g_N B_z + a_{1,-}^{zz})/a_{1,-}^{zx}] \pm \arctan[(\sigma \mu_N g_N B_z + a_{n,\pm}^{zz})/a_{n,\pm}^{zx}]$. The relative tilt angle $\Delta\varphi$ formalizes that driving to the AS conserving the nuclear-spin state will lead to a nuclear spin precession in the AS until the state decays back to the GS.

This interaction of the nuclear-spin eigenstates of the GS in the AS can be used to polarize the nuclear spin. A suitable domain for this may be $\Delta\varphi \neq 0$, but $\Delta\varphi \ll 1$ where we can approximate the eigenstates of the AS using first-order perturbation theory. The eigenstates of the ancillary KD pseudospin σ (in the principal axis system of the GS KD down state) are

$$|n, \pm, \sigma, m\rangle \approx |n, \pm, \sigma\rangle \left[|I, m\rangle - \frac{\Delta\varphi}{2} \sqrt{I(I+1) - m(m+1)} |I, m+1\rangle + \frac{\Delta\varphi}{2} \sqrt{I(I+1) - m(m-1)} |I, m-1\rangle \right]. \quad (26)$$

The form of these states shows the possibility to resonantly drive the transitions from the GS σ, m state to the corresponding $\sigma, m \pm 1$ from where the decay mainly occurs to the $\sigma, m \pm 1$ GS state (if $\Delta\varphi \ll 1$). Here, the small angle $\Delta\varphi$ ensures that the main decay does not decrease the nuclear magnetic moment again, while still enabling a resonant drive of the polarizing transition. This process polarizes the nuclear spin stepwise. The outlined approach works with the transition to an ES or the second GS, given that the nuclear transition lines can be resolved. This is in contrast to the proposed zero-strain protocol, where a pseudospin flipping transition in combination with the correct polarization renders this requirement unnecessary.

While we focused for concreteness on one additional example including strain in this paper, we note that combining

our model with the general approach outlined in Ref. [46], protocols optimized for different scenarios can be developed that are best matched to the technical setup.

IV. CONCLUSION

We studied the influence of strain on TM defects in SiC, focusing on a particularly promising center for quantum technology applications, the substitutional vanadium defect at the k site of 4H-SiC. We found that using strain enables the engineering of the electronic g tensor and optical selection rules, thereby opening the possibility for strain-controlled manipulation (microwave gates) within the KDs, as well as Λ and V optical three-level setups where both branches can be driven using the same polarization. By combining strain

and magnetic fields, we showed a path towards engineering Λ systems for the pseudospin states of the KD, thus enabling further prospects such as state preparation within the GS KD. We also discussed the prospect of state readout of strained defects using cycling transitions.

Furthermore, we showed the influence of strain on the hyperfine interaction within the KDs. Here, we found that the previously proposed polarization protocol is likely not applicable anymore for strongly strained samples. Therefore, we discussed one example of an application of our theory where it is straightforward to find different polarization schemes even in the presence of strain. A natural next step would be to exploit our theoretical insights in future experiments.

ACKNOWLEDGMENTS

We acknowledge funding from the European Union's Horizon 2020 research and innovation program under Grant Agreement No. 862721 (QuanTELCO). B.T. and G.B. additionally acknowledge funding from the German Federal Ministry of Education and Research (BMBF) under Grant Agreement No. 13N16212 (SPINNING). A.G. acknowledges the support by the National Excellence Program for the project of quantum-coherent materials (NKFIH Grant No. KKP129866) as well as by the Ministry of Culture and Innovation and the National Research, Development and Innovation Office within the Quantum Information National Laboratory of Hungary (Grant No. 2022-2.1.1-NL-2022-00004). A.G. additionally acknowledges the high-performance computational resources provided by KIFÜ (Governmental Agency for IT Development) institute of Hungary and the European Commission for project QuMicro (Grant No. 101046911).

APPENDIX A: DFT CALCULATION METHODS

We model the vanadium defect embedded in a 128-atom 4H-SiC supercell. Its electronic structure is calculated using the plane-wave based VIENNA AB-INITIO SIMULATION PACKAGE [72–75], with the Γ -point approximation for the k -point sampling. The plane-wave cutoff is set to 420 eV and PAW method [76] is used for the core electrons. We apply DFT using the hybrid exchange functional of Heyd, Scuseria, and Ernzerhof (HSE06) [77] with on-site correction (DFT + U) according to the Dudarev-approach [78], where the d orbitals of the vanadium atom is effected by $U = -2.5$ eV [79]. The atomic configurations are relaxed to forces smaller than 0.01 eV/Å. A size convergence test in a 576-atom supercell was performed in the ground state, validating the applied method. Excited state electronic configurations are calculated with the constrained occupation Δ -SCF method [80]. The methods for applying strain are discussed in Ref. [47]. We note that the local defect structure is relaxed within the strain constraint applied to the lattice.

The results of this simulation are discussed in the main text and we additionally provided all slopes extracted for the coupling to strain in Table II. In this table, $s_{nm}^{y^{(o)}}$ takes the same role as $s_{nm}^{x^{(o)}}$ [see Eq. (11)] but takes into account that we cannot assume them to be the same *a priori* within the DFT calculation. We encode the slope of the ES- and GS-level

TABLE II. Calculated strain-orbital coupling coefficients extracted from linear perturbation model of the orbital level splitting and ZPL energies from DFT. Coupling strengths to strain perturbations which transform according to x and y basis elements of the irreducible representation E are equal within computational accuracy. Standard deviations are extracted from the linear fit and are given in parenthesis for the last meaningful digit. We note that the $s_{22}^z, s_{22}^{z'}$ values correspond to the slope of the ES-GS splitting, where we chose $s_{11}^{z'}, s_{11}^z = 0$.

Symmetry	Parameter	Calculated value (eV/strain)
x of E	s_{11}^x	1.04(1)
	s_{22}^x	0.56(5)
	$s_{11}^{x'}$	0.94(2)
	$s_{22}^{x'}$	0.85(2)
	s_{22}^y	1.037(2)
y of E	s_{11}^y	0.582(2)
	s_{22}^y	0.958(4)
	$s_{11}^{y'}$	0.84(1)
	$s_{22}^{y'}$	1.9(1)
	s_{22}^z	1.26(8)
A_1	s_{22}^z	
	$s_{22}^{z'}$	

splitting in $s_{22}^z, s_{22}^{z'}$ by choosing $s_{11}^z, s_{11}^{z'} = 0$, as we discuss in the main text.

APPENDIX B: CRYSTAL FIELD EIGENSTATES AND SIGNS OF THE STRAIN COUPLING CONSTANTS

Inside the d orbital projections, the crystal eigenstates are given as

$$\begin{aligned} |\pm_1\rangle &= \cos(\phi) |\pm 1\rangle \mp \sin(\phi) |\mp 2\rangle, \\ |\pm_2\rangle &= -\sin(\phi) |\pm 1\rangle \mp \cos(\phi) |\mp 2\rangle, \end{aligned} \quad (\text{B1})$$

where the crystal mixing angle ϕ describes the admixture of states that transform equally under C_{3v} .

In the absence of spin-orbit coupling, the doublet states split due to x, y strain, we use this to determine the sign of the strain coupling constants. The eigenvectors for purely ϵ_{nm}^x strain are (within the doublet projection) given by

$$\begin{aligned} \frac{|+1\rangle \pm |-1\rangle}{\sqrt{2}} &= \cos(\phi) (|+1\rangle \pm |-1\rangle) \\ &\quad - \sin(\phi) (|-2\rangle \mp |+2\rangle), \end{aligned} \quad (\text{B2})$$

$$\begin{aligned} \frac{|+2\rangle \pm |-2\rangle}{\sqrt{2}} &= -\sin(\phi) (|+1\rangle \pm |-1\rangle) \\ &\quad - \cos(\phi) (|-2\rangle \mp |+2\rangle), \end{aligned} \quad (\text{B3})$$

with the eigenvalues $\epsilon_n \pm \epsilon_{nm}^x$. We note the parallel of these pairs of states to the cubic harmonics $|x^2 - y^2\rangle = \frac{1}{\sqrt{2}}(|+2\rangle + |-2\rangle)$, $|xy\rangle = \frac{i}{\sqrt{2}}(-|+2\rangle + |-2\rangle)$, $|xz\rangle = \frac{1}{\sqrt{2}}(-|+1\rangle + |-1\rangle)$, $|yz\rangle = \frac{i}{\sqrt{2}}(|+1\rangle + |-1\rangle)$, and $|z^2\rangle = |0\rangle$. With this, we find that the strain eigenstates are proportional to the distinct sets of cubic harmonics $|+n\rangle + |-n\rangle \propto |yz\rangle, |xy\rangle$ and $|+n\rangle - |-n\rangle \propto |xz\rangle, |x^2 - y^2\rangle$.

With this, we can obtain the sign of the coupling from the DFT simulation without spin by comparing the projection

on the cubic harmonics (of the d orbital). We find that for $\epsilon_{xz} = 0.01$ in the GS (ES), the lower energy state is mainly $|xz\rangle$ ($|xy\rangle$), i.e., the $|+1\rangle - |-1\rangle$ ($|+1\rangle + |-1\rangle$) state, such that $s_{11}^x > 0$ ($s_{22}^x < 0$). Analogously, for $\epsilon_{yy} - \epsilon_{xx} = 0.01$ in the GS (ES), the lower energy state is mainly $|xz\rangle$ ($|xy\rangle$), i.e., the $|+1\rangle - |-1\rangle$ ($|+2\rangle + |-2\rangle$) state, such that $s_{11}^x > 0$ ($s_{22}^x < 0$).

Due to the known transformation properties of the states from the literature (using the difference in the hyperfine tensor), we assign the lower KD of the GS in the absence of strain to Γ_4 and in the ES to $\Gamma_{5/6}$ [36,40,41,44,46]. To accommodate this in the model, we use that for the vanadium defect in the k site in 4H-SiC, $\lambda_{11}^z > 0$ and $\lambda_{22}^z < 0$.

APPENDIX C: HIGHER-ORDER EFFECTS

To understand higher order effects, we treat a purely x -type strain using a Schrieffer-Wolff transformation [81]. To this

end, we perturbatively take block off-diagonal elements of the spin-orbit and strain Hamiltonians (together) into account. We do the following calculations in the basis where the leading-order doublet Hamiltonians $P_n H_{\text{ezf}} P_n$ given in Eq. (15) are diagonalized, such that we can afterwards directly study the corrections affecting the KDs. Then we use the transformation $U = \exp(-S)$ and, within first-order perturbation theory,

$$S = \sum_{n \neq m} P_n (H_{\text{so}} + H_{\text{st}}) P_m / (\epsilon_n - \epsilon_m), \quad (\text{C1})$$

where we directly neglect spin-orbit and strain terms in the denominator as they are part of the higher (neglected) orders. The corrections to the zero-field energies are then given by

$\frac{1}{2} [S, H_{\text{ezf}}]$, which is block diagonal in the KDs and corrects their energies by

$$E_{n,-}' = (-1)^n \frac{\lambda_{12}^z/4 + \lambda_{12}^x \sin^2(\theta_n/2) + \epsilon_{12}^x}{\epsilon_2 - \epsilon_1} - \frac{\lambda_{13}^x \cos^2(\theta_n/2) + \epsilon_{13}^x (1 + \sin(\theta_n))}{\epsilon_3 - \epsilon_1}, \quad (\text{C2})$$

$$E_{n,+}' = (-1)^n \frac{\lambda_{12}^z/4 + \lambda_{12}^x \cos^2(\theta_n/2) + \epsilon_{12}^x}{\epsilon_2 - \epsilon_1} - \frac{\lambda_{13}^x \sin^2(\theta_n/2) + \epsilon_{13}^x (1 - \sin(\theta_n))}{\epsilon_3 - \epsilon_1}, \quad (\text{C3})$$

$$E_3' = \frac{\lambda_{23}^x + 2\epsilon_{23}^x}{\epsilon_3 - \epsilon_2} + \frac{\lambda_{13}^x + 2\epsilon_{13}^x}{\epsilon_3 - \epsilon_1}, \quad (\text{C4})$$

where $n = 1, 2$.

In addition to this, the corresponding corrections of the remaining parts h of the full Hamiltonian can be calculated as $[S, h]$. For instance, this corrects the coupling to a magnetic field along the crystal axis \vec{e}_z projected onto the KDs as

$$H_{n,-}^z = \left[(-1)^n \frac{2\lambda_{12}^z}{\epsilon_2 - \epsilon_1} S_z - \frac{4\lambda_{12}^x \sin^2(\theta_n/2)}{\epsilon_2 - \epsilon_1} S_x \right] r_{12}^z \mu_B B_z, \quad (\text{C5})$$

$$H_{n,+}^z = \left[(-1)^n \frac{2\lambda_{12}^z}{\epsilon_2 - \epsilon_1} S_z - \frac{4\lambda_{12}^x \cos^2(\theta_n/2)}{\epsilon_2 - \epsilon_1} S_x \right] r_{12}^z \mu_B B_z, \quad (\text{C6})$$

$$H_3^z = 0, \quad (\text{C7})$$

where one can neglect the off-diagonal matrix elements considering that they are suppressed by the leading-order term $g_s S_z$, as we expect for $g_s \gg r_{12}^z$. While in this paper, we focus on providing the straightforward recipe to calculate higher-order terms for simplicity, previous work

takes higher-order effects in the spin-orbit coupling only (without strain) into account [43,44,46]. Analogously, expressions for other magnetic-field directions and parts of the Hamiltonian can be calculated using S but are omitted here.

- [1] I. Aharonovich, D. Englund, and M. Toth, Solid-state single-photon emitters, *Nat. Photon.* **10**, 631 (2016).
- [2] K. Heshami, D. G. England, P. C. Humphreys, P. J. Bustard, V. M. Acosta, J. Nunn, and B. J. Sussman, Quantum memories: emerging applications and recent advances, *J. Mod. Opt.* **63**, 2005 (2016).
- [3] D. Awschalom, K. K. Berggren, H. Bernien, S. Bhave, L. D. Carr, P. Davids, S. E. Economou, D. Englund, A. Faraon, M. Fejer, S. Guha, M. V. Gustafsson, E. Hu, L. Jiang, J. Kim, B. Korzh, P. Kumar, P. G. Kwiat, M. Lončar, M. D. Lukin, *et al.*, Development of quantum interconnects (quics) for next-

generation information technologies, *PRX Quantum* **2**, 017002 (2021).

- [4] X.-F. He, N. B. Manson, and P. T. H. Fisk, Paramagnetic resonance of photoexcited N-V defects in diamond. I. level anticrossing in the 3A ground state, *Phys. Rev. B* **47**, 8809 (1993).
- [5] T. Gaebel, M. Domhan, I. Popa, C. Wittmann, P. Neumann, F. Jelezko, J. R. Rabau, N. Stavrias, A. D. Greentree, S. Praver, J. Meijer, J. Twamley, P. R. Hemmer, and J. Wrachtrup, Room-temperature coherent coupling of single spins in diamond, *Nat. Phys.* **2**, 408 (2006).

- [6] L. Childress, M. V. G. Dutt, J. M. Taylor, A. S. Zibrov, F. Jelezko, J. Wrachtrup, P. R. Hemmer, and M. D. Lukin, Coherent dynamics of coupled electron and nuclear spin qubits in diamond, *Science* **314**, 281 (2006).
- [7] C. Santori, P. Tamarat, P. Neumann, J. Wrachtrup, D. Fattal, R. G. Beausoleil, J. Rabeau, P. Olivero, A. D. Greentree, S. Praver, F. Jelezko, and P. Hemmer, Coherent population trapping of single spins in diamond under optical excitation, *Phys. Rev. Lett.* **97**, 247401 (2006).
- [8] A. Gali, M. Fyta, and E. Kaxiras, *Ab initio* supercell calculations on nitrogen-vacancy center in diamond: Electronic structure and hyperfine tensors, *Phys. Rev. B* **77**, 155206 (2008).
- [9] S. Felton, A. M. Edmonds, M. E. Newton, P. M. Martineau, D. Fisher, D. J. Twitchen, and J. M. Baker, Hyperfine interaction in the ground state of the negatively charged nitrogen vacancy center in diamond, *Phys. Rev. B* **79**, 075203 (2009).
- [10] J. R. Maze, A. Gali, E. Togan, Y. Chu, A. Trifonov, E. Kaxiras, and M. D. Lukin, Properties of nitrogen-vacancy centers in diamond: The group theoretic approach, *New J. Phys.* **13**, 025025 (2011).
- [11] G. D. Fuchs, G. Burkard, P. V. Klimov, and D. D. Awschalom, A quantum memory intrinsic to single nitrogen-vacancy centres in diamond, *Nat. Phys.* **7**, 789 (2011).
- [12] E. Togan, Y. Chu, A. Imamoglu, and M. D. Lukin, Laser cooling and real-time measurement of the nuclear spin environment of a solid-state qubit, *Nature (London)* **478**, 497 (2011).
- [13] C. G. Yale, B. B. Buckley, D. J. Christle, G. Burkard, F. J. Heremans, L. C. Bassett, and D. D. Awschalom, All-optical control of a solid-state spin using coherent dark states, *Proc. Natl. Acad. Sci. USA* **110**, 7595 (2013).
- [14] D. A. Golter, K. N. Dinyari, and H. Wang, Nuclear-spin-dependent coherent population trapping of single nitrogen-vacancy centers in diamond, *Phys. Rev. A* **87**, 035801 (2013).
- [15] L. Busaite, R. Lazda, A. Berzins, M. Auzinsh, R. Ferber, and F. Gahbauer, Dynamic ^{14}N nuclear spin polarization in nitrogen-vacancy centers in diamond, *Phys. Rev. B* **102**, 224101 (2020).
- [16] S. S. Hegde, J. Zhang, and D. Suter, Efficient quantum gates for individual nuclear spin qubits by indirect control, *Phys. Rev. Lett.* **124**, 220501 (2020).
- [17] M. W. Doherty, N. B. Manson, P. Delaney, F. Jelezko, J. Wrachtrup, and L. C. L. Hollenberg, The nitrogen-vacancy colour centre in diamond, *Phys. Rep.* **528**, 1 (2013).
- [18] D. Suter and F. Jelezko, Single-spin magnetic resonance in the nitrogen-vacancy center of diamond, *Prog. Nucl. Magn. Reson. Spectrosc.* **98-99**, 50 (2017).
- [19] S. Pezzagna and J. Meijer, Quantum computer based on color centers in diamond, *Appl. Phys. Rev.* **8**, 011308 (2021).
- [20] G. Thiering and A. Gali, Theory of the optical spin-polarization loop of the nitrogen-vacancy center in diamond, *Phys. Rev. B* **98**, 085207 (2018).
- [21] A. Gruber, A. Dräbenstedt, C. Tietz, L. Fleury, J. Wrachtrup, and C. von Borczyskowski, Scanning confocal optical microscopy and magnetic resonance on single defect centers, *Science* **276**, 2012 (1997).
- [22] P. J. Wellmann, Review of SiC crystal growth technology, *Semicond. Sci. Technol.* **33**, 103001 (2018).
- [23] J. Liu, Z. Xu, Y. Song, H. Wang, B. Dong, S. Li, J. Ren, Q. Li, M. Rommel, X. Gu, B. Liu, M. Hu, and F. Fang, Confocal photoluminescence characterization of silicon-vacancy color centers in 4H-SiC fabricated by a femtosecond laser, *Nanotechnol. Precis. Eng.* **3**, 218 (2020).
- [24] A. Chakravorty, B. Singh, H. Jataw, R. Meena, D. Kanjilal, and D. Kabiraj, Controlled generation of photoemissive defects in 4H-SiC using swift heavy ion irradiation, *J. Appl. Phys.* **129**, 245905 (2021).
- [25] B.-S. Song, T. Asano, S. Jeon, H. Kim, C. Chen, D. D. Kang, and S. Noda, Ultrahigh-Q photonic crystal nanocavities based on 4H silicon carbide, *Optica* **6**, 991 (2019).
- [26] D. M. Lukin, C. Dory, M. A. Guidry, K. Y. Yang, S. D. Mishra, R. Trivedi, M. Radulaski, S. Sun, D. Vercruyssen, G. H. Ahn, and J. Vučković, 4H-silicon-carbide-on-insulator for integrated quantum and nonlinear photonics, *Nat. Photon.* **14**, 330 (2020).
- [27] M. A. Guidry, K. Y. Yang, D. M. Lukin, A. Markosyan, J. Yang, M. M. Fejer, and J. Vučković, Optical parametric oscillation in silicon carbide nanophotonics, *Optica* **7**, 1139 (2020).
- [28] C. Bekker, M. J. Arshad, P. Cilibrizzi, C. Nikolatos, P. Lomax, G. S. Wood, R. Cheung, W. Knolle, N. Ross, B. Gerardot, and C. Bonato, Scalable fabrication of hemispherical solid immersion lenses in silicon carbide through grayscale hard-mask lithography, *Appl. Phys. Lett.* **122**, 173507 (2023).
- [29] M. Radulaski, M. Widmann, M. Niethammer, J. L. Zhang, S.-Y. Lee, T. Rendler, K. G. Lagoudakis, N. T. Son, E. Janzén, T. Ohshima, J. Wrachtrup, and J. Vučković, Scalable quantum photonics with single color centers in silicon carbide, *Nano Lett.* **17**, 1782 (2017).
- [30] J. Wang, Y. Zhou, X. Zhang, F. Liu, Y. Li, K. Li, Z. Liu, G. Wang, and W. Gao, Efficient generation of an array of single silicon-vacancy defects in silicon carbide, *Phys. Rev. Appl.* **7**, 064021 (2017).
- [31] E. Sörman, N. T. Son, W. M. Chen, O. Kordina, C. Hallin, and E. Janzén, Silicon vacancy related defect in 4H and 6H SiC, *Phys. Rev. B* **61**, 2613 (2000).
- [32] E. Janzén, A. Gali, P. Carlsson, A. Gällström, B. Magnusson, and N. Son, The silicon vacancy in SiC, *Phys. B: Condens. Matter* **404**, 4354 (2009).
- [33] R. Nagy, M. Widmann, M. Niethammer, D. B. R. Dasari, I. Gerhardt, O. O. Soykal, M. Radulaski, T. Ohshima, J. Vučković, N. T. Son, I. G. Ivanov, S. E. Economou, C. Bonato, S.-Y. Lee, and J. Wrachtrup, Quantum properties of dichroic silicon vacancies in silicon carbide, *Phys. Rev. Appl.* **9**, 034022 (2018).
- [34] A. Gali, A. Gällström, N. T. Son, and E. Janzén, Theory of neutral divacancy in SiC: A defect for spintronics, in *Silicon Carbide and Related Materials 2009*, Materials Science Forum, Vol. 645 (Trans Tech Publications Ltd., Baech, Switzerland, 2010), pp. 395–397.
- [35] A. L. Falk, B. B. Buckley, G. Calusine, W. F. Koehl, V. V. Dobrovitski, A. Politi, C. A. Zorman, P. X.-L. Feng, and D. D. Awschalom, Polytype control of spin qubits in silicon carbide, *Nat. Commun.* **4**, 1819 (2013).
- [36] P. Cilibrizzi, M. J. Arshad, B. Tissot, N. T. Son, I. G. Ivanov, T. Astner, P. Koller, M. Ghezellou, J. Ul-Hassan, D. White, C. Bekker, G. Burkard, M. Trupke, and C. Bonato, Ultra-narrow inhomogeneous spectral distribution of telecom-wavelength vanadium centres in isotopically-enriched silicon carbide, *Nat. Commun.* **14**, 8448 (2023).
- [37] T. Bosma, G. J. J. Lof, C. M. Gilardoni, O. V. Zwier, F. Hendriks, B. Magnusson, A. Ellison, A. Gällström, I. G. Ivanov, N. T. Son, R. W. A. Havenith, and C. H. van der Wal,

- Identification and tunable optical coherent control of transition-metal spins in silicon carbide, *npj Quantum Inf.* **4**, 48 (2018).
- [38] L. Spindlberger, A. Cs  r  , G. Thiering, S. Putz, R. Karhu, J. U. Hassan, N. T. Son, T. Fromherz, A. Gali, and M. Trupke, Optical properties of vanadium in 4H silicon carbide for quantum technology, *Phys. Rev. Appl.* **12**, 014015 (2019).
- [39] C. M. Gilardoni, T. Bosma, D. van Hien, F. Hendriks, B. Magnusson, A. Ellison, I. G. Ivanov, N. T. Son, and C. H. van der Wal, Spin-relaxation times exceeding seconds for color centers with strong spin–orbit coupling in SiC, *New J. Phys.* **22**, 103051 (2020).
- [40] G. Wolfowicz, C. P. Anderson, B. Diler, O. G. Poluektov, F. J. Heremans, and D. D. Awschalom, Vanadium spin qubits as telecom quantum emitters in silicon carbide, *Sci. Adv.* **6**, eaaz1192 (2020).
- [41] T. Astner, P. Koller, C. M. Gilardoni, J. Hendriks, N. T. Son, I. G. Ivanov, J. U. Hassan, C. H. v. d. Wal, and M. Trupke, Vanadium in silicon carbide: Telecom-ready spin centres with long relaxation lifetimes and hyperfine-resolved optical transitions, *arXiv:2206.06240*.
- [42] A. Cs  r   and A. Gali, *Ab initio* determination of pseudospin for paramagnetic defects in SiC, *Phys. Rev. B* **102**, 241201(R) (2020).
- [43] B. Tissot and G. Burkard, Spin structure and resonant driving of spin-1/2 defects in SiC, *Phys. Rev. B* **103**, 064106 (2021).
- [44] B. Tissot and G. Burkard, Hyperfine structure of transition metal defects in SiC, *Phys. Rev. B* **104**, 064102 (2021).
- [45] C. M. Gilardoni, I. Ion, F. Hendriks, M. Trupke, and C. H. van der Wal, Hyperfine-mediated transitions between electronic spin-1/2 levels of transition metal defects in SiC, *New J. Phys.* **23**, 083010 (2021).
- [46] B. Tissot, M. Trupke, P. Koller, T. Astner, and G. Burkard, Nuclear spin quantum memory in silicon carbide, *Phys. Rev. Res.* **4**, 033107 (2022).
- [47] P. Udvarhelyi, V. O. Shkolnikov, A. Gali, G. Burkard, and A. P  lyi, Spin-strain interaction in nitrogen-vacancy centers in diamond, *Phys. Rev. B* **98**, 075201 (2018).
- [48] P. Udvarhelyi and A. Gali, *Ab initio* spin-strain coupling parameters of divacancy qubits in silicon carbide, *Phys. Rev. Appl.* **10**, 054010 (2018).
- [49] P. Udvarhelyi, G. Thiering, N. Morioka, C. Babin, F. Kaiser, D. Lukin, T. Ohshima, J. Ul-Hassan, N. T. Son, J. Vu  kovi  , J. Wrachtrup, and A. Gali, Vibronic states and their effect on the temperature and strain dependence of silicon-vacancy qubits in 4H-SiC, *Phys. Rev. Appl.* **13**, 054017 (2020).
- [50] P. Udvarhelyi, T. Clua-Provost, A. Durand, J. Li, J. H. Edgar, B. Gil, G. Cassabo  s, V. Jacques, and A. Gali, A planar defect spin sensor in a two-dimensional material susceptible to strain and electric fields, *npj Comput. Mater.* **9**, 150 (2023).
- [51] M. Koppenh  fer, C. Padgett, J. V. Cady, V. Dharod, H. Oh, A. C. Bleszynski Jayich, and A. A. Clerk, Single-spin readout and quantum sensing using optomechanically induced transparency, *Phys. Rev. Lett.* **130**, 093603 (2023).
- [52] S. Meesala, Y.-I. Sohn, B. Pingault, L. Shao, H. A. Atikian, J. Holzgrafe, M. G  ndo  an, C. Stavarakas, A. Sipahigil, C. Chia, R. Evans, M. J. Burek, M. Zhang, L. Wu, J. L. Pacheco, J. Abraham, E. Bielejec, M. D. Lukin, M. Atat  re, and M. Lon  ar, Strain engineering of the silicon-vacancy center in diamond, *Phys. Rev. B* **97**, 205444 (2018).
- [53] C. T. Nguyen, D. D. Sukachev, M. K. Bhaskar, B. Machielse, D. S. Levonian, E. N. Knall, P. Stroganov, C. Chia, M. J. Burek, R. Riedinger, H. Park, M. Lon  ar, and M. D. Lukin, An integrated nanophotonic quantum register based on silicon-vacancy spins in diamond, *Phys. Rev. B* **100**, 165428 (2019).
- [54] P. Ouartchaiyapong, K. W. Lee, B. A. Myers, and A. C. B. Jayich, Dynamic strain-mediated coupling of a single diamond spin to a mechanical resonator, *Nat. Commun.* **5**, 4429 (2014).
- [55] J. Teissier, A. Barfuss, P. Appel, E. Neu, and P. Maletinsky, Strain coupling of a nitrogen-vacancy center spin to a diamond mechanical oscillator, *Phys. Rev. Lett.* **113**, 020503 (2014).
- [56] A. Barfuss, M. Kasprczyk, J. K  lbl, and P. Maletinsky, Spin-stress and spin-strain coupling in diamond-based hybrid spin oscillator systems, *Phys. Rev. B* **99**, 174102 (2019).
- [57] According to previous DFT results, the k site corresponds to the α configuration of vanadium in 4H-SiC [42].
- [58] J. R. Dietz and E. L. Hu, Optical and strain stabilization of point defects in silicon carbide, *Appl. Phys. Lett.* **120**, 184001 (2022).
- [59] L. Robledo, L. Childress, H. Bernien, B. Hensen, P. F. A. Alkemade, and R. Hanson, High-fidelity projective read-out of a solid-state spin quantum register, *Nature (London)* **477**, 574 (2011).
- [60] A. Delteil, W. B. Gao, P. Fallahi, J. Miguel-Sanchez, and A. Imamog  lu, Observation of quantum jumps of a single quantum dot spin using submicrosecond single-shot optical readout, *Phys. Rev. Lett.* **112**, 116802 (2014).
- [61] D. D. Sukachev, A. Sipahigil, C. T. Nguyen, M. K. Bhaskar, R. E. Evans, F. Jelezko, and M. D. Lukin, Silicon-vacancy spin qubit in diamond: A quantum memory exceeding 10 ms with single-shot state readout, *Phys. Rev. Lett.* **119**, 223602 (2017).
- [62] M. Raha, S. Chen, C. M. Phenicie, S. Ourari, A. M. Dibos, and J. D. Thompson, Optical quantum nondemolition measurement of a single rare earth ion qubit, *Nat. Commun.* **11**, 1605 (2020).
- [63] M. H. Appel, A. Tiranov, A. Javadi, M. C. L  bl, Y. Wang, S. Scholz, A. D. Wieck, A. Ludwig, R. J. Warburton, and P. Lodahl, Coherent spin-photon interface with waveguide induced cycling transitions, *Phys. Rev. Lett.* **126**, 013602 (2021).
- [64] H. R. Gray, R. M. Whitley, and C. R. Stroud, Coherent trapping of atomic populations, *Opt. Lett.* **3**, 218 (1978).
- [65] X. Xu, B. Sun, P. R. Berman, D. G. Steel, A. S. Bracker, D. Gammon, and L. J. Sham, Coherent population trapping of an electron spin in a single negatively charged quantum dot, *Nat. Phys.* **4**, 692 (2008).
- [66] W. R. Kelly, Z. Dutton, J. Schlafer, B. Mookerji, T. A. Ohki, J. S. Kline, and D. P. Pappas, Direct observation of coherent population trapping in a superconducting artificial atom, *Phys. Rev. Lett.* **104**, 163601 (2010).
- [67] C. Dong, V. Fiore, M. C. Kuzyk, and H. Wang, Optomechanical dark mode, *Science* **338**, 1609 (2012).
- [68] M. Demirplak and S. A. Rice, Adiabatic population transfer with control fields, *J. Phys. Chem. A* **107**, 9937 (2003).
- [69] M. V. Berry, Transitionless quantum driving, *J. Phys. A: Math. Theor.* **42**, 365303 (2009).
- [70] D. Gu  ry-Odelin, A. Ruschhaupt, A. Kiely, E. Torrontegui, S. Mart  n  ez-Garaot, and J. G. Muga, Shortcuts to adiabaticity: Concepts, methods, and applications, *Rev. Mod. Phys.* **91**, 045001 (2019).
- [71] J. Hendriks, C. M. Gilardoni, C. Adambukulam, A. Laucht, and C. H. v. d. Wal, Coherent spin dynamics of hyperfine-coupled vanadium impurities in silicon carbide, *arXiv:2210.09942*.

- [72] G. Kresse and J. Hafner, *Ab initio* molecular dynamics for liquid metals, *Phys. Rev. B* **47**, 558 (1993).
- [73] G. Kresse and J. Furthmüller, Efficient iterative schemes for *ab initio* total-energy calculations using a plane-wave basis set, *Phys. Rev. B* **54**, 11169 (1996).
- [74] G. Kresse and J. Furthmüller, Efficiency of ab-initio total energy calculations for metals and semiconductors using a plane-wave basis set, *Comput. Mater. Sci.* **6**, 15 (1996).
- [75] J. Paier, M. Marsman, K. Hummer, G. Kresse, I. C. Gerber, and J. G. Ángyán, Screened hybrid density functionals applied to solids, *J. Chem. Phys.* **124**, 154709 (2006).
- [76] P. E. Blöchl, Projector augmented-wave method, *Phys. Rev. B* **50**, 17953 (1994).
- [77] A. V. Krukau, O. A. Vydrov, A. F. Izmaylov, and G. E. Scuseria, Influence of the exchange screening parameter on the performance of screened hybrid functionals, *J. Chem. Phys.* **125**, 224106 (2006).
- [78] S. L. Dudarev, G. A. Botton, S. Y. Savrasov, C. J. Humphreys, and A. P. Sutton, Electron-energy-loss spectra and the structural stability of nickel oxide: An LSDA+U study, *Phys. Rev. B* **57**, 1505 (1998).
- [79] V. Ivády, I. A. Abrikosov, E. Janzén, and A. Gali, Role of screening in the density functional applied to transition-metal defects in semiconductors, *Phys. Rev. B* **87**, 205201 (2013).
- [80] A. Gali, E. Janzén, P. Deák, G. Kresse, and E. Kaxiras, Theory of spin-conserving excitation of the NV⁻ center in diamond, *Phys. Rev. Lett.* **103**, 186404 (2009).
- [81] S. Bravyi, D. P. DiVincenzo, and D. Loss, Schrieffer-Wolff transformation for quantum many-body systems, *Ann. Phys.* **326**, 2793 (2011).